Biomedical Signal Processing and Control 102 (2025) 107327

Contents lists available at ScienceDirect

Biomedical Signal Processing and Control

journal homepage: www.elsevier.com/locate/bspc

ROMP-DCP: Dictionary learning via regularized orthogonal matching pursuit and difference of convex programming for robust fluorescence molecular tomography

Linzhi Su [a], Huimin Gao [a], Limin Chen [a], Wenlong Tang [a], Yi Chen [a,b,*], Chengyi Gao [c], Huangjian Yi [a], Xin Cao [a,*]

[a] School of Information Science and Technology, Northwest University, Xi'an, Shaanxi 710127, China
[b] School of Electrical and Mechanical Engineering, The University of Adelaide, Adelaide, SA 5005, Australia
[c] Department of Oncology, The First Affiliated Hospital, Xi'an Jiaotong University, Xi'an, Shaanxi 710061, China

ARTICLE INFO

Keywords:
Fluorescence molecular tomography
Regularized orthogonal matching pursuit
Difference of convex programming
Inverse problem

ABSTRACT

Fluorescence molecular tomography (FMT) is a cost-effective, high-resolution imaging technique that offers non-invasive 3D visualization of targets labeled with fluorescent probes. However, challenges arise due to light scattering and absorption and the complexity of inverse problems, which hinder accurate reconstruction of fluorescence distribution. To overcome these challenges and enhance the accuracy of fluorescence distribution reconstruction, we propose a sparse reconstruction method based on dictionary learning via regularized orthogonal matching pursuit and difference of convex programming (ROMP-DCP). ROMP-DCP implements the dictionary learning strategy using an alternating optimization scheme. During the sparse coding phase, the ROMP algorithm is adopted to ensure sparsity in line with internal light source distribution characteristics. In the dictionary update stage, the incorporation of the difference of convex (DC) programming and the DC algorithm ensures convergence and robustness. Through this ROMP-DCP approach, it effectively adapts to the intrinsic structure of the data and captures its sparse features, thereby achieving more accurate and sparser FMT reconstruction results. The results of numerical simulation experiments indicate that ROMP-DCP method obtains the most accurate reconstruction results. Furthermore, the effectiveness of our method was further demonstrated in the *in vivo* experiments. ROMP-DCP has the smallest localization error (LE), with a value of 0.369 mm. In comparison, the other three methods have higher values: IVTCG is at 0.544 mm, ROMP at 0.702 mm, and HTPA at 0.962 mm. In addition, ROMP-DCP method also has the highest Dice similarity coefficient (DICE), which is 0.648. Overall, ROMP-DCP holds significant potential for improving the reconstruction accuracy and stability of FMT in biomedical applications.

1. Introduction

Fluorescence molecular imaging (FMI), a technique widely used in preclinical and clinical research, employs fluorescently labeled molecules to visualize the distribution and activity of specific targets within biological organisms [1–3]. For FMI, an external excitation light source is required to stimulate the fluorescent molecular probes, inducing them to emit fluorescence. These fluorescent signals are detected, allowing the acquisition of molecular information within the body [4]. FMI is characterized by its high sensitivity, high specificity, and non-invasive property, making it suitable for detecting fluorescence sources in biological tissues. However, FMI provides 2D imaging and is limited to capturing fluorescence distribution information on the surface of objects [5]. As an extension of FMI, fluorescence molecular tomography (FMT) utilizes reconstruction algorithms to enable 3D imaging of fluorescent probes distribution within biological tissues [6,7], providing information about the internal structure and function. Today, FMT is widely applied in biomedical research and preclinical diagnostics, providing a crucial non-invasive imaging tool for disease diagnosis, treatment monitoring, and drug development [8–10].

Although FMT holds significant advantages, it still faces significant challenges regarding imaging quality and measurement accuracy in

* Corresponding authors.
E-mail addresses: yichen.cgz@gmail.com (Y. Chen), caoxin918@hotmail.com (X. Cao).

https://doi.org/10.1016/j.bspc.2024.107327
Received 10 August 2024; Received in revised form 19 November 2024; Accepted 8 December 2024
Available online 16 December 2024

biological tissues [11–13]. Firstly, the strong scattering effect of photons creates a nonlinear relationship between surface measurements of fluorescence signals and the distribution of internal fluorescence sources, and the simplified photon propagation model affects detection accuracy [14]. Secondly, during the FMT reconstruction process, background noise, such as the autofluorescence emitted by the biological body itself, can also significantly affect the accuracy of the imaging. Additionally, the limited information from surface measurements compared to unknown internal sources results in an ill-posed inverse reconstruction problem, where the number of equations is insufficient for the unknowns, potentially leading to non-unique solutions [15].

To address these issues effectively and ensure accurate and stable reconstruction results, various effective strategies have been proposed by researchers. An effective strategy is to improve the accuracy of the photon propagation model. In the reconstruction of FMT, incorporating detailed anatomical structure information provided by computed tomography (CT) or magnetic resonance imaging (MRI) can significantly enhance its accuracy [16]. CT yields density data of bones and soft tissues, while MRI offers detailed soft tissue structure, facilitating the precise simulation of photon scattering and absorption across different tissues. Another category of methods addresses the ill-posedness of the inverse problem by utilizing a regularization framework, effectively narrowing down the space of feasible solutions. Tikhonov regularization is a widely applied optimization method that enhances the stability of solutions by adding an L_2-norm [17], but it may lead to a loss of detail and over-smoothing [18]. Furthermore, L_1-norm regularization is commonly introduced into the objective function to impose sparse constraints [19]. The L_1-norm can be viewed as a convex relaxation of the L_0-norm [20],which promotes sparsity during the image reconstruction [21]. However, the linear sparsity penalty of L_1-norm may overly constrain weaker features, leading to the loss of important features in FMT reconstruction. In contrast, L_p-norm $(0 < p < 1)$ can control sparsity in a wider range and handle sparse signals more flexibly. When $p < 1$, L_p-norm is more effective than L_1-norm in promoting sparsity, resulting in more accurate solutions during FMT reconstruction [22,23].Notably, most traditional regularization methods typically require the selection of an appropriate regularization parameter through extensive experience and experimentation.

In recent years, deep learning has shown broad application prospects in FMT [24,25], enhancing FMT reconstruction quality and data processing efficiency. Huang et al. proposed a deep convolutional neural network (DCNN) [26], which alleviates errors caused by grid registration in traditional methods to some extent. Zhang et al. proposed a new 3D fusion dual-sampling deep learning network model (UHR-DeepFMT) to achieve ultra-high spatial resolution reconstruction in FMT [27]. However, deep learning techniques have certain limitations in practical applications. In the training of network models, it is necessary to generate different training datasets for different imaging objects [15]. Additionally, due to the inability to obtain a large amount of *in vivo* data, researchers often rely on simulated data to drive their research.

In addition to deep learning methods, some researchers have combined compressed sensing (CS) theory with greedy algorithms for FMT reconstruction. The stagewise orthogonal matching pursuit (StOMP) is proposed to construct a sparse solution by selecting multiple eligible atoms at each iteration [19]. Compared to StOMP, the regularized orthogonal matching pursuit (ROMP) algorithm [28] more effectively approximates the original signal while ensuring sparsity, through a better atom-selection method. However, traditional greedy algorithms primarily focus on sparsity constraints and do not fully consider the structural characteristics of signals within subspaces [29]. Therefore, these methods suffer from serious issues such as inaccurate reconstruction of light source positions, low morphological similarity, and instability. To overcome these challenges, we incorporated a dictionary learning (DL) strategy [30,31] into our method. DL is essentially an optimization problem based on the iterative update between the dictionary and sparse coding [32]. Since sparsity is typically measured by the L_0-norm, this leads to a non-convex optimization problem, increasing the difficulty of solving it. Research has shown that difference of convex programming (DCP) can decompose non-convex function into the difference of two convex functions [33], transforming the problem into a more manageable form. To further address the convex optimization problem and enhance the interrelationships between atoms, we developed the DC algorithm (DCA) [34]. This algorithm adjusts the directions of the atoms in the dictionary through an optimization process, allowing for better adaptation to the characteristics of the data. By using this method to train a dictionary for the given fluorescence distribution data, we can more effectively capture the unique features and intrinsic structure of the signals, thereby enhancing the recovery of sparse signals. It considers both the sparsity of the signal and the relationship between atoms, making the recovery process more efficient and precise. Its adaptability and accuracy contribute to achieving higher-resolution FMT reconstruction from limited data.

A sparse reconstruction method based on dictionary learning via regularized orthogonal matching pursuit and difference of convex programming (ROMP-DCP) for robust FMT is proposed in this paper. The main contributions of this paper can be highlighted as follows:

(1) We effectively combine the ROMP algorithm and the DCP method through the DL strategy. The DL algorithm in this paper employs an alternating iterative method to optimize the sparse coding and dictionary update phases.
(2) In the sparse coding phase, the ROMP algorithm combines greedy strategy and regularization mechanism to ensure sparse and accurate reconstruction, enhancing noise robustness by selecting inner products with similar magnitudes.
(3) In the dictionary update phase, we employ DCP to avoid direct handling of a non-convex function by only processing its convex components. The developed DCA optimizes the dictionary atoms, enabling a better representation of the data and leading to more accurate and sparse reconstruction results for the fluorescence distribution.
(4) We have analyzed and systematically summarized the computational complexity of the ROMP-DCP algorithm to better elucidate its efficiency, highlighting the contributions of each stage in the process.
(5) To evaluate the comprehensive performance of our proposed ROMP-DCP method, we conducted a series of numerical simulation experiments and *in vivo* experiments. Experimental results show that ROMP-DCP outperforms other methods in terms of localization error (LE) and Dice similarity coefficient (DICE).

The structure of this paper is organized as follows: In Section 2, we introduce the FMT forward model, the FMT inverse problem, and the ROMP-DCP method. In Section 3, we describe the details and results of the numerical simulations and *in vivo* experiments. In Section 4, we discuss the work presented in this paper. In Section 5, we illustrate the challenges of this study and outline future research directions. In Section 6, we provide the conclusion of the paper.

2. Methodology

2.1. Forward problem

The complex structure of biological tissues leads to various intricate phenomena during the propagation of near-infrared light, including reflection, absorption, scattering, and refraction. In FMT imaging, the radiative transfer equation (RTE) [35] is commonly used to describe the propagation of photons in biological tissues. The time-domain expression of the light propagation model constructed through the RTE is presented in [15]. However, the RTE is typically a complex integral–differential equation that is challenging to solve directly. Typically,

computational resources are limited, and FMT is a rapid imaging technique, which has certain requirements for imaging time [36]. Therefore, researchers have proposed some simplified and approximate forms of the RTE, including: the diffusion equation (DE) [37], the simplified spherical harmonics (SP_N) [38], etc. The DE, as a low-order RTE approximation model, is simple to solve and suitable for tissues with high scattering and low absorption, and it is more commonly used in practical applications. The propagation process of photons described by DE is defined as follows:

$$\begin{cases} \nabla\cdot[D_x(r)\nabla\Phi_x(r)] - \mu_{ax}(r)\Phi_x(r) = -\Theta\delta(r-r_s) & (r\in\Omega) \\ \nabla\cdot[D_m(r)\nabla\Phi_m(r)] - \mu_{am}(r)\Phi_m(r) = -\Phi_x(r)\eta\mu_{af}(r) & (r\in\Omega) \end{cases} \tag{1}$$

Here, ∇ denotes the gradient operator, and Ω represents the domain of the imaged object. The parameters μ_{ax}, μ_{sx} represent the absorption and scattering coefficients at the excitation wavelength, while μ_{am},μ_{sm} represent the absorption and scattering coefficients at the emission wavelength. D_x and D_m are the optical diffusion coefficients for the excitation and emission processes, respectively, defined as $D_{x,m} = 1/3(\mu_{ax,am}+(1-G)\mu_{sx,sm})$, where G is the anisotropy parameter [39]. $\Phi_x(r)$ and $\Phi_m(r)$ respectively represent the photon flux during the excitation and emission processes. $\Theta\delta(r-r_s)$ denotes the excitation light source, where Θ is the light source intensity. $\eta\mu_{af}(r)$ represents the fluorescence yield to be recovered.

By introducing Robin-type boundary conditions to solve the coupled DE, we have:

$$2D_{x,m}(r)\nabla\Phi_{x,m}(r) + q\Phi_{x,m}(r) = 0(r\in\partial\Omega) \tag{2}$$

Here, $\partial\Omega$ denotes the boundary of the biological tissue, and q is a constant representing the refractive index difference between the biological tissue surface and the air. It can be approximated as $q\approx\frac{1+R}{1-R}$, and $R = -1.4399n^{-2}+0.7099n^{-1}+0.6681+0.0636n$. For a non-contact FMT imaging system, n is approximately equal to 1.4 [29].To solve the differential Eq. (1) with the Robin boundary condition (2), we use the finite element method (FEM). This approach establishes a linear relationship between the surface measurement data and the unknown fluorescence yield:

$$AX = B \tag{3}$$

where $A\in R^{M\times N}(M\ll N)$ represents the system weight matrix, $X = (X_1, X_2, \cdots X_N)^T \in R^{N\times 1}$ denotes the distribution of the internal fluorescence sources to be reconstructed, and $B = (b_1, b_2, \cdots b_N)^T \in R^{M\times 1}$ represents the measured fluorescence distribution on the surface. Some notations used in this paper are summarized in Table 1, and some acronyms and abbreviations used in this paper are listed in Table 2.

2.2. DCP and DCA

DCP and DCA are used to solve non-convex optimization problems [40,41], forming the foundation of global optimization and non-convex programming, originally proposed by Tao in 1985. DCP decomposes complex non-convex optimization problems into a series of easily solvable convex subproblems [42], while DCA progressively approaches the optimal solution of the original problem by alternately minimizing these convex subproblems. Within the framework of DCP, the original non-convex problem is decomposed into the difference of two convex functions, and the optimization form is as follows:

$$minf(x) = f_1(x) - f_2(x)(x\in R^n) \tag{4}$$

where $f(x)$ is a non-convex function in R^n, and $f_1(x)$ and $f_2(x)$ are lower semi-continuous strictly convex functions. The function $f(x)$ is referred to as a DC function, and $f_1(x)$,$f_2(x)$ can be considered the DC components of the DC function. Through this decomposition, we can iteratively solve a series of convex subproblems to address non-convexity.

Table 1
Notations used in this paper.

Notations	Description
$A\in R^{M\times N}(M\ll N)$	System weight matrix
$X\in R^{N\times 1}$	Sparse representation vector
$B\in R^{M\times 1}$	Measured fluorescence photon distribution
M	Row number of system weight matrix A and fluorescence photon distribution B
Ω	The domain of the imaged object
N	Column number of system weight matrix and row number of sparse representation vector
S	Sparsity level
a_j	Column vectors of matrix A
$D_{x,m}$	Diffusion coefficients for excitation and emission
μ_{ax} ,μ_{sx}	Absorption and scattering coefficients at excitation wavelength
μ_{am} , μ_{sm}	Absorption and scattering coefficients at emission wavelength
$r^{(k)}$	Residual vector at the k iteration
A^T, $(A)^{-1}$, $tr(A)$	Transpose of a matrix A,the inverse of matrix A and trace of a matrix A
$I^{(k)}$	The column index set I of matrix A at the k iteration
P	Correlation coefficients
$f(x)$	Expression of a function
$\langle x,h\rangle$	The inner product of two sequence x,h
$\odot$	The component-wise product
$\|\cdot\|_0$, $\|\cdot\|_1$, $\|\cdot\|_2$	L_0-norm, L_1-norm, L_2-norm

Table 2
Acronyms and abbreviations.

Abbreviations	Full name
FMT	Fluorescence molecular tomography
FMI	Fluorescence molecular imaging
CT	Computed tomography
ROMP	Regularized orthogonal matching pursuit
DC	Difference of convex
DCP	Difference of convex programming
DCA	Difference of convex algorithm
DL	Dictionary learning
ROMP-DCP	Regularized orthogonal matching pursuit and difference of convex programming
IVTCG	Incomplete variable truncated conjugate gradient
HTPA	Half thresholding Pursuit algorithm
CS	Compressed sensing
2D,3D	Two-dimensional, three-dimensional
RTE	Radiative Transfer Equation
DE	Diffusion equation
LE	localization error
DICE	Dice similarity coefficient

In each iteration k, the DCA approximates the concave part $f_2(x)$ at the current point x^k using its affine minorization $g(x)$, thereby solving the convex optimization problem [43]. Specifically, $g(x)$ is defined as:

$$g(x) = f_2(x^{(k)}) + \left\langle x - x^{(k)}, h^{(k)} \right\rangle \tag{5}$$

Where $h^{(k)}\in\partial f_2(x^{(k)})$. The minorization process yields the following form of convex programming:

$$x^{(k+1)} \in argminf_1(x) - g(x)$$

$$\Leftrightarrow x^{(k+1)} \in argmin\ \ f_1(x) - \left\langle x, h^{(k)} \right\rangle \tag{6}$$

By pursuing the minimization of the above convex function in each iteration, we ultimately obtain the optimal solution for problem (1), which is $x^{(k+1)}$. The DCA is summarized as **Algorithm 1**.

Algorithm 1: DCA

Initialization: $x^{(0)}\in R^n$, iteration $k = 1$
Iteration Process:

(*continued on next page*)

(*continued*)

Algorithm 1: DCA

While $k < k_{max}$ do
1): Calculate $h^{(k)} \in \partial f_2(x^{(k)})$
2): Calculate $x^{(k+1)} \in argmin\ f_1(x) - \left\langle x, h^{(k)} \right\rangle$
3):$k = k + 1$
4): Until convergence of $x^{(k)}$ or meet the max iteration.
End while

It is worth mentioning that DCA is a descent algorithm that ensures global convergence without the need for line search, and it has the following key properties [44,45]:

(1) If $f_1(x^{(k+1)}) - f_2(x^{(k+1)}) = f_1(x^{(k)}) - f_2(x^{(k)})$, then $x^{(k)}$ is a critical point of $f_1(x) - f_2(x)$, and the algorithm terminates at the k th iteration.
(2) If the optimal value of problem (4) is finite and the sequence $\{x^{(k)}\}$ is bounded, then every limit point $\{x^{(k)}\}$ is a critical point of $f_1(x) - f_2(x)$.
(3) DCA converges linearly for general DC programs.
(4) DCA has a finite convergence for polyhedral DC programs. If $f_2(x)$ is polyhedral and differentiable at x^*, then x^* is a local optimizer of $f_1(x) - f_2(x)$.

DCA guarantees that the value of the objective function decreases progressively at each iteration. If the objective function is bounded below, the iterative sequence will converge to a local optimum or a stationary point. This ensures the convergence and stability of the algorithm [46]. A more comprehensive and in-depth understanding of DCA can be found in [47,48]. From this, we can conclude that DCA is an effective algorithm for solving non-convex models.

2.3. Reconstruction based on ROMP-DCP method

The inverse problem in FMT is to determine the 3D distribution of the light source to be reconstructed based on a known forward problem model of light propagation. During the imaging process, light is absorbed and scattered within biological tissues, making the obtained solutions often unstable and non-unique. This results in severe ill-posed of the inverse reconstruction problem. In our research, we represent the sparsity constraint in FMT reconstruction using L_0 regularization, defined as follows:

$$\frac{1}{2} argmin \|AX - B\|_2^2 s.t. \|X\|_0 \le S \tag{7}$$

where $\|X\|_0$ denotes the L_0-norm, and S is an integer that can be used to adjust the sparsity level of the reconstruction result. In this paper, FMT reconstruction is formulated as a dictionary learning problem. The system matrix A can be regarded as an overcomplete dictionary, X represents the weight coefficients of the column vectors in the dictionary, and B is the result of the linear combination of the column vectors in matrix A. Eq. (7) for A and X is typically non-convex. Therefore, we adopt an iterative alternating strategy for DL, solving the problem through two stages: the sparse coding stage and the dictionary update stage. This process starts with an initialized dictionary and then repeatedly executes these two stages until convergence. The sparse coding stage employs the ROMP algorithm, which is known for its strong stability and high efficiency. In FMT construction, the internal light source distribution is typically small and sparse [49]. The ROMP algorithm ensures that only a few of the most representative atoms are selected to capture these sparse signals, thereby maintaining the sparsity of the fluorescent source distribution. In the dictionary update stage, the dictionary sparse optimization problem is effectively solved using methods based on DCP and DCA.DCP decomposes the non-convex objective function into the difference of two convex functions, and subsequently, DCA adjusts the direction of atoms in dictionary A by solving two convex optimization problems in each iteration, allowing them to better adapt to the features of matrix B.

2.3.1. The space coding stage

At this stage, by initializing and fixing the dictionary A, the sparse representation X of the measurement vector B is generated. The objective optimization function can be expressed as:

$$\frac{1}{2} \underset{X \in R^{N \times 1}}{argmin} \|B - AX\|_2^2 \ \ s.t. \ \ \|X\|_0 \le S. \tag{8}$$

Drawing on the use of typical greedy algorithms in compressive sensing for signal reconstruction, we employ the ROMP algorithm to achieve sparse representation in FMT. The ROMP algorithm combines the speed and ease of use advantages of greedy algorithms with the robustness of convex programming methods. Moreover, it introduces regularization constraints during the greedy iteration process, enabling the recovery of non-zero values from uncertain measurements with a maximum of S iterations. In each iteration, ROMP selects a group of atoms with similar magnitudes and updates the residual through an orthogonalization step [50], ensuring that the sparse solution accurately reflects the internal light source distribution.

When the sparsity level S is known, firstly, according to the principle of correlation, we select the S largest values from the correlation coefficients P. If the number of non-zero values is less than S, then we select all non-zero values and store their corresponding indices in the set J. Here, the calculation of correlation coefficients P is as follows:

$$P = \underset{j}{argmax} \|A_j^T r^{(k-1)}\|_1 \tag{9}$$

where j represents the column vectors of matrix A $(1 \le j \le N)$, and each column can be seen as an atom, denoted as a_j. $r^{(k-1)}$ represents the residual vector at the $(k-1)$ iteration.

Next, according to the regularization principle, the atoms are grouped, and the atom with the maximum energy is added to the subset J_0. Specifically, the correlation coefficients of the atoms corresponding to the indices in set J are grouped, and from these groups, the indices of the atoms corresponding to the group with the maximum energy are selected and stored in set J_0. J_0 satisfies:

$$|P(i)| \le 2|P(j)| \forall i,j \in J_0 \tag{10}$$

Then, update the column index set I and the related column set $A^{(k)}$ of matrix A, as follows:

$$\begin{cases} I^{(k)} = I^{(k-1)} \cup J_0 \\ A^{(k)} = A^{(k-1)} \cup a_j \end{cases} \forall i,j \in J_0 \tag{11}$$

Finally, use the least squares method to obtain the approximate solution and update the residual vector. The calculation method is as follows:

$$\begin{cases} X^{(k)} = \underset{x}{argmin} |B - A^{(k)} X^{(k)}| = \left(A^{(k)^T} A^{(k)}\right)^{-1} A^{(k)^T} B \\ r^{(k)} = B - A^{(k)} X^{(k)} = B - A^{(k+1)} \left(A^{(k)^T} A\right)^{-1} A^{(k)^T} B \end{cases} \tag{12}$$

Through this iterative update process, ensuring that the reconstructed signal matches the characteristics of the fluorescent source distribution. It is worth mentioning that the number of column vectors in matrix $A^{(k)}$ is generally not S, because we impose a constraint $\|I^{(k)}\|_0 \ge 2S$ during the regularization and atom selection process. Therefore, the number of column vectors in $A^{(k)}$ usually does not exceed 3 S.

2.3.2. The dictionary update stage

In the dictionary update stage, the objective optimization function can be expressed as:

$$\frac{1}{2}\underset{A}{argmin}\|B-AX\|_2^2 s.t.\|X\|_0 \le S. \tag{13}$$

By fixing the sparse vector X, the solution to problem (13) is obtained as:

$$\underset{A\in\mathscr{C}}{min}\frac{1}{2}tr\left(A^TAXX^T\right)-tr\left(A^TBX^T\right) \tag{14}$$

$$\mathscr{C}=\left\{A\in R^{M\times N}:\|a_j\|=1\forall j=1,2,...,N\right\}$$

Here, we introduce a convex term $f_1(A)$ to solve (14) through DC decomposition. The expression for $f_1(A)$ is as follows:

$$f_1(A)=\frac{1}{2}\sum_{j=1}^{n}\rho_j\|a_j\|^2 \tag{15}$$

where ρ is an $N\times 1$ dimensional column vector, with each element equal to $\left|XX^T\right|$, and a_j is the column vector of matrix A.

Let $P=XX^T$, $Q=BX^T$, we obtain the DC decomposition as follows:

$$\begin{cases} f_1(A)=\frac{1}{2}\sum_{j=1}^{n}\rho_j\|a_j\|^2 \\ f_2(A)=\frac{1}{2}\sum_{j=1}^{n}\rho_j\|a_j\|^2-\left(\frac{1}{2}tr\left(A^TAP\right)-tr\left(A^TQ\right)\right) \end{cases} \tag{16}$$

By this decomposition, DCP solves convex optimization problems in each iteration, gradually converging to a sparse solution. Adopting the DCA from **Algorithm 1**, Calculate $H^{(k-1)}\in\partial f_2(A^{(k-1)})$, we obtain the following solution:

$$\begin{aligned} H^{(k-1)}&=\nabla f_2\left(A^{(k-1)}\right) \\ H^{(k-1)}&=D\odot A^{(k-1)}-\left(A^{(k-1)}P-Q\right) \end{aligned} \tag{17}$$

where $D\in R^{M\times N}$ is defined such that each row equals ρ. $\odot$ represents an element-wise multiplication operation, where the elements at corresponding positions in two matrices are multiplied to form a new matrix.

Then, we calculate $A^{(k)}$ by optimizing the following function:

$$A^{(k)}\in\underset{A}{argmin}\left\{f_1(A)-\left\langle A,H^{(k-1)}\right\rangle\right\} \tag{18}$$

Each column of the matrix H is represented by $h_j(j=1,2,...,N)$. The calculation is as follows:

$$\begin{aligned} A^{(k)}&=\underset{A}{argmin}\left\{f_1(A)-tr\left(H^{(k-1)^T}A^{(k-1)}\right)\right\} \\ A^{(k)}&=\underset{A}{argmin}\sum_{j=1}^{n}\left(\frac{1}{2}\rho_j\|a_j\|^2-\left\langle a_j,h_j^{(k-1)}\right\rangle\right) \end{aligned} \tag{19}$$

In the dictionary update stage, the formula for updating the column vectors of matrix A is as follows:

$$a_j^{(k)}=\frac{h_j^{(k-1)}}{max=\left\{\rho_j,\|h_j^{(k-1)}\|\right\}} \tag{20}$$

The optimization process gradually adjusts the atoms in the dictionary, allowing them to better adapt to the features of the input data B. This dictionary update strategy captures the intrinsic structure and sparsity of the signal, thereby improving the accuracy of sparse signal recovery. We combine ROMP and DCP through the DL strategy, enabling more effective capture of the sparse characteristics of internal light sources in the FMT reconstruction process, while maintaining sensitivity to signal details. To summarize, the flowchart of the ROMP-DCP method is presented in **Algorithm 2**.

Algorithm 2: ROMP-DCP for FMT reconstruction

Input: Measured fluorescence photon distribution $B\in R^{M\times 1}$, system matrix $A\in R^{M\times N}$, sparsity level S.

(*continued on next column*)

(*continued*)

Algorithm 2: ROMP-DCP for FMT reconstruction

Initialization: $X^{(0)}=0$, $tol=1e-5$, residual vector $r^{(0)}=B$, index set $I^{(0)}=\varnothing$, index column matrix $A^{(0)}=\varnothing$, iteration $k=1$, the maximum number of iterations $k_{max}=100$.
While $\|X^k-X^{k-1}\|_2>tol$ or $k<k_{max}$ do
Step 1: Sparse coding stage
1): Identify: Calculate observation vector and store the corresponding index J through the Eq. (9).
2): Regularize: Choose the set J_0 with the maximal energy through the Eq. (10).
3): Update: Update index sets and atoms, obtain the approximate solution and complete the update of residual through the Eq. (11), Eq. (12).
4): Stop criterion: until $k>S$ or $\|I^{(k)}\|_0\ge 2S$ or $r^{(k)}=0$, then stop the iteration.
Step 2: Dictionary update stage
1: Compute $P=X^{(k)}X^{(k)^T}$, $Q=BX^{(k)^T}$.
2: Compute $H^{(k-1)}\in\partial f_2(A^{(k-1)})$ through the Eq. (17).
3: **for** $j=1$ *to* N *do*
1): Update the column of matrix through the Eq. (20).
2): Normalizing $a_j^{(k)}=\frac{a_j^{(k)}}{\|a_j^{(k)}\|}$
End for
Step 3: $k=k+1$
End while
Output: $X=X^{(k)}$

2.4. Complexity analysis of the ROMP-DCP algorithm

Since each iteration of ROMP-DCP is performed in two stages, the computational complexity of the algorithm is analyzed separately for the sparse coding stage and the dictionary update stage. The computational complexity of **Algorithm 2** depends on the following parameters: the sparsity level S (where S is a positive integer), the number of dictionary rows M, and the number of dictionary columns N, with $M\ll N$. In the sparse coding stage, the ROMP algorithm selects the dictionary atoms that best match the fluorescence distribution data to construct a sparse representation. This process requires calculating an $M\times N$ matrix and solving a least squares problem, resulting in the computational complexity of $O(NS^2+MN)$. In the dictionary update stage, the computational complexity is primarily determined by terms such as XX^T, BX^T, and AXX^T, which involve matrix multiplications essential for refining the dictionary atoms. Thereby, the complexity is $O(N^2+MN+MN^2)$. Nonetheless, the algorithm benefits from the convergence properties of DCP technology, enabling it to achieve stable solutions within a manageable number of iterations.

3. Experiment and results

In this section, to evaluate the performance of the proposed ROMP-DCP method in FMT reconstruction, we designed several sets of numerical simulation experiments and *in vivo* experiments. We compared the ROMP-DCP method with the incomplete variable truncated conjugate gradient method (IVTCG) based on L_1-norm [51], the ROMP algorithm based on L_0-norm [28], and the half thresholding Pursuit algorithm (HTPA) based on $L_{1/2}$-norm [52]. Comparisons were made with IVTCG, ROMP, and HTPA algorithms in terms of localization accuracy, morphological recovery, robustness, and practicality. All processes were implemented in MATLAB (2021b) on a laptop equipped with an Intel(R) Core(TM) i7-8550U CPU (1.80 GHz) and 8 GB RAM.

3.1. Evaluation metrics

To assess the performance of different reconstruction algorithms in source localization and shape recovery, this study employs two commonly used quantitative metrics: localization error (LE) and Dice similarity coefficient (DICE).

LE is the Euclidean distance between the reconstructed source center (x_r,y_r,z_r) and the actual source center (x_t,y_t,z_t). The calculation for-

mula is as follows:

$$LE = \sqrt{(x_r - x_t)^2 + (y_r - y_t)^2 + (y_r - y_t)^2} \tag{21}$$

where the LE value is always positive, and a smaller LE value indicates that the reconstruction result is closer to the actual position, thus reflecting higher reconstruction localization accuracy.

The DICE is a metric that measures the shape similarity between the reconstructed source and the true source. The calculation formula is as follows:

$$DICE = \frac{2|X_r \cap Y_t|}{|X_r| + |X_t|} \tag{22}$$

where X_r represents the actual source region and Y_t represents the reconstructed source region. It evaluates the similarity between the two source regions by calculating the degree of overlap. A value closer to 1 indicates a higher shape similarity, while a value closer to 0 indicates a lower shape similarity.

3.2. Experimental setup

3.2.1. Numerical simulation experiments

A series of numerical simulation experiments were conducted based on a cylindrical heterogeneous model with a radius of 10 mm and a height of 30 mm to validate the performance of the algorithm. The model consisted of five biological organs: muscle, heart, bone, lung, and liver, as shown in Fig. 1(A). Each region is represented by different colors, corresponding to these different organs. According to the relevant work by Hou et al. [53], the optical parameters of each organ at 650 nm in the model are presented in Table 3.

In the cylindrical heterogeneous model, the single-source experiment simulates an actual fluorescent source by setting a homogeneous sphere with a radius of 1 mm at (−2, −5, 5) mm. The dual-source experiment simulates actual fluorescent sources by setting two homogeneous spheres, each with a radius of 1 mm, at the positions (−5, −5, 7) mm and (−5, −5, 17) mm, respectively. In the noise resistance experiment, Gaussian noise levels of 5 %, 10 %, 15 %, 20 %, and 25 % were sequentially added to the single-source experiment to observe changes in reconstruction performance, evaluating the accuracy and robustness of ROMP-DCP.

During the FMT reconstruction process, we typically use a tetrahedral mesh structure of the physical model to highlight the discretization process in the forward simulation. The establishment of the mesh provides a foundation for subsequent light propagation calculations. Therefore, we used Comsol Multiphysics software to segment the model into a tetrahedral mesh [54]. This mesh consisted of 4626 nodes and 25,840 tetrahedral elements, as shown in Fig. 1(B). When performing optical simulations of biological tissues, the molecular optical simulation environment (MOSE) based on the Monte Carlo method [55] is often used. It can simulate the actual optical properties and morphological characteristics of biological tissues. Fig. 1(C) shows the forward simulation results for the single-source, used to obtain the surface fluorescence distribution, facilitating the subsequent reconstruction of the internal fluorescence distribution through the algorithm. The simulation results display the distribution of light intensity emitted from the source, with different color regions indicating varying light intensities.

3.2.2. In vivo experiment

To further evaluate the feasibility and practicality of ROMP-DCP for *in vivo* imaging, we conducted *in vivo* experiments according to the protocol approved by the Animal Ethics Committee of Northwest University of China. The experiment involved a female BALB/c nude mouse, using an FMT/CT dual-modality imaging system with a transmission optical path. This system provides both anatomical and optical information. By integrating multi-angle fluorescence images with CT data, we estimated the location of *in vivo* fluorescence target and optimized the feasible region settings. The imaging system structure is illustrated in Fig. 2. The experimental process is as follows:

The initial step involved injecting a 1 mm-radius spherical fluorescent bead into a Cy5.5 fluorescent dye solution, which was then implanted into the abdominal cavity of the mouse to serve as a fluorescent target. The mouse was anesthetized with an appropriate anesthetic and placed on a rotating stage to ensure stability during the experiment. A 650 nm continuous wave semiconductor laser was employed to excite the fluorescent target. Subsequently, fluorescence data were collected from the surface of the organism using a highly sensitive EMCCD camera (IxonUltra888). These data were essential for generating clear fluorescence images, which is a critical step for visualizing the fluorescent distribution and ensuring the accuracy of subsequent analysis.

After the fluorescence imaging, the mouse underwent imaging with a Micro-CT system to acquire detailed anatomical and tissue structure information. CT imaging provided an important anatomical reference for fluorescence imaging and facilitated the precise localization of the fluorescent target, enhancing the comprehensive analysis value of the imaging results.

Next, we segmented the anatomical structures of major organs, including muscles, heart, lungs, stomach, liver, and kidneys, and integrated them into the mouse model. Finally, the 2D fluorescence images were mapped onto the 3D mouse model surface through registration points. We discretized the mouse model into 3057 nodes and 16,627 tetrahedral elements for FMT reconstruction. The 3D view of the mouse model is shown in Fig. 3(A). Its tetrahedral mesh is shown in Fig. 3(B). The actual implanted source center position was (9.5, 14, 18) mm. To

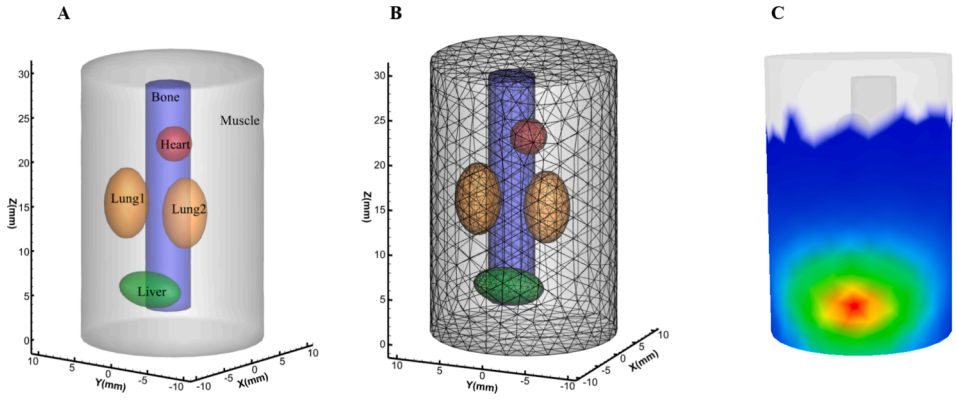

Fig. 1. (A) The 3D view of the cylindrical heterogeneous model. (B) The tetrahedral mesh of the physical model. (C) The forward simulation result of the single-source.

Table 3
Optical parameters of organs in a nonhomogeneous cylinder at 650 **nm**.

Tissue	$\mu_{ax}(r)\,[mm^{-1}]$	$\mu_{sx}(r)\,[mm^{-1}]$	$\mu_{am}(r)\,[mm^{-1}]$	$\mu_{sm}(r)\,[mm^{-1}]$	g
Muscle	0.0052	10.80	0.0068	10.30	0.90
Heart	0.0083	6.733	0.0104	6.60	0.85
Bone	0.0060	60.09	0.0030	30.74	0.90
Lungs	0.0133	19.70	0.0203	19.50	0.90
Liver	0.0329	7.00	0.0176	6.60	0.90

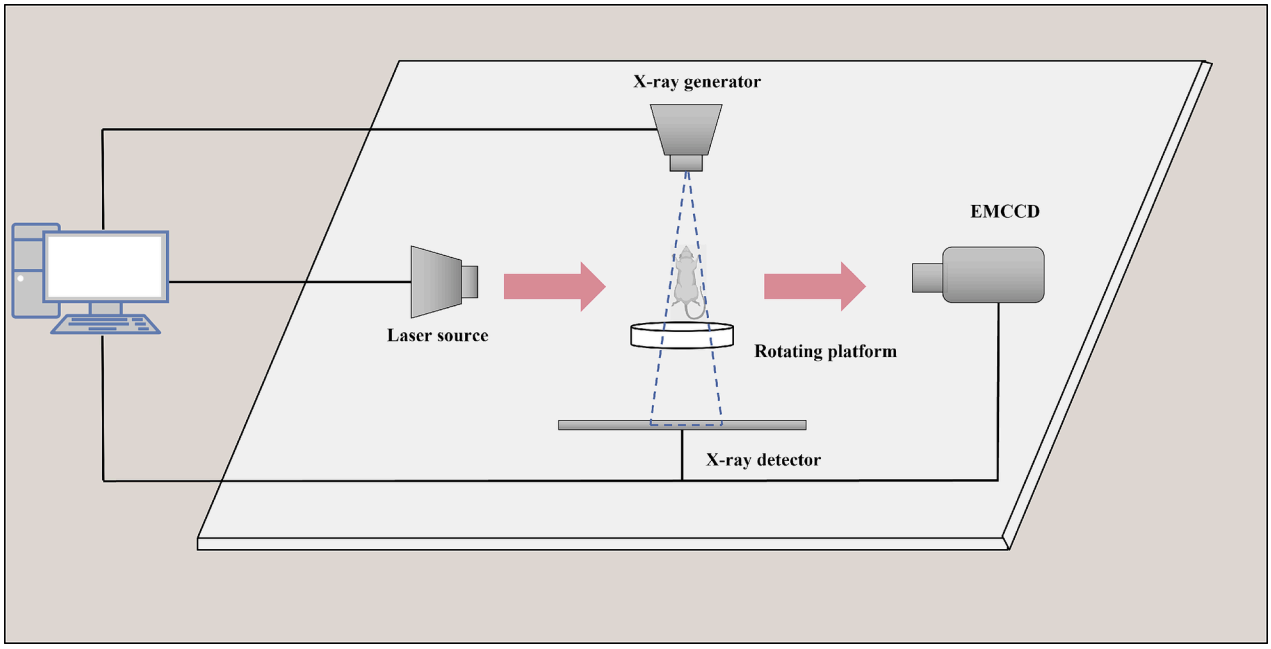

Fig. 2. The principal diagram of the FMT/CT imaging system.

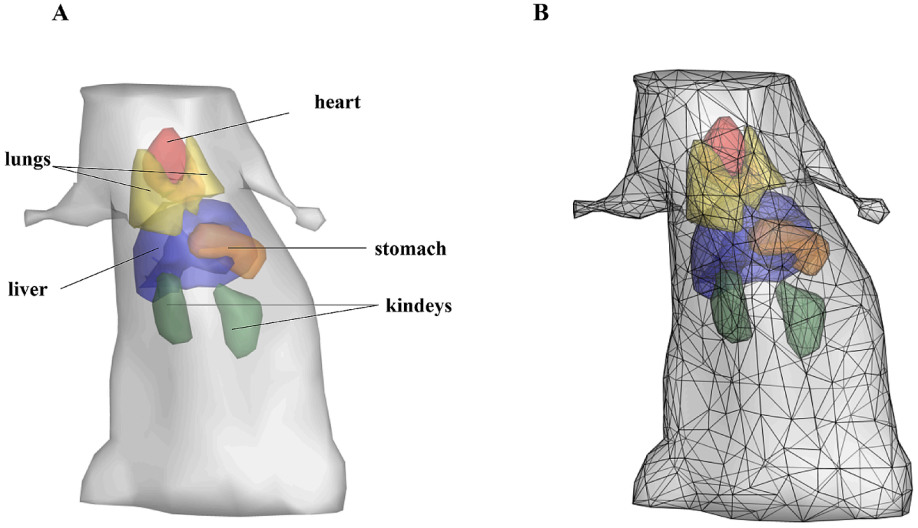

Fig. 3. (A) The 3D view of the mouse model. (B) The 3D view of the tetrahedral mesh.

evaluate the practicality of ROMP-DCP *in vivo* experiment, we compared it with the other three algorithms.

3.3. Experimental setup

3.3.1. Single-source simulation results

In the single-source spherical simulation experiment, the IVTCG, ROMP, and HTPA algorithms were compared with our ROMP-DCP algorithm. The 3D views of the reconstructed results and the reconstructed slice views at the Z = 5 mm plane are shown in Fig. 4.

In the 3D views, the reconstructed fluorescence sources are displayed as cyan-colored regions. In the slice views, the white circles represent the actual positions and areas of the light sources, while the cyan areas depict the reconstructed sources. Table 4 summarizes the quantitative

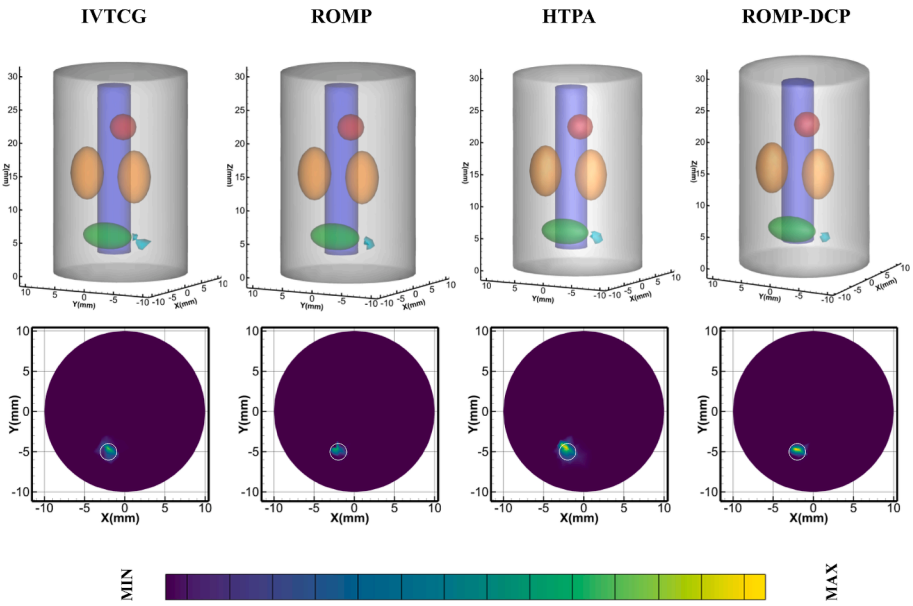

Fig. 4. The reconstruction results of single-source using four different methods.

Table 4
Quantitative results in single-source simulation reconstruction experiment.

Method	Actual source center (mm)	Reconstructed source center (mm)	LE (mm)	DICE
IVTCG	(−2, −5, 5)	(−2.216, −4.492, 5.016)	0.553	0.452
ROMP		(−2.292, −4.389, 5.350)	0.763	0.556
HTPA		(−2.402, −4.341, 5.206)	0.792	0.365
ROMP-DCP		(−2.051, −4.714, 5.170)	0.337	0.872

analysis results of the four algorithms. From the experimental results, it can be observed that our proposed ROMP-DCP algorithm outperforms the IVTCG, ROMP, and HTPA methods. Specifically, ROMP-DCP has the LE of 0.337 mm, which is significantly lower than the LE values of the other methods: 0.553 mm for IVTCG, 0.763 mm for ROMP, and 0.792 mm for HTPA. This lower LE indicates that the reconstructed light source positions are closer to the actual positions, showcasing the accuracy of our algorithm. Additionally, ROMP-DCP achieves the highest DICE of 0.872, reflecting its superior ability to recover the shape of the source region. In contrast, IVTCG has a DICE of 0.452, ROMP has a DICE of 0.556, and HTPA has the lowest DICE of 0.365. These results suggest that while the other methods provide reasonable localization, they struggle with accurately reconstructing the source shape. In summary, the ROMP-DCP algorithm demonstrates both robust localization and effective shape recovery.

3.3.2. *Dual-source simulation results*

To further evaluate the performance of ROMP-DCP under more complex scenarios, we conducted dual-source experiments using different algorithms. Fig. 5 shows the 3D reconstruction results and longitudinal slice display results of the dual-source experiment, while Table 5 presents the quantitative analysis results of the aforementioned methods.

The experimental results demonstrate that the ROMP-DCP method achieves the smallest total LE, with a value of 0.814 mm. Like the HTPA algorithm, the total LE is 2.115 mm, indicating that the localization accuracy is poor. The reconstruction results of the IVTCG and ROMP algorithms show that the signal sources are overly sparse, whereas the reconstruction results of the ROMP-DCP algorithm are closest to the actual signal sources. Additionally, the DICE value is also the highest compared to the other algorithms. This value indicates a robust overlap between the reconstructed regions and the actual fluorescence source regions, with the ROMP-DCP method achieving substantial accuracy in shape recovery. In contrast, the DICE values for the two light sources reconstructed by the ROMP algorithm were 0.480 and 0.393, respectively, revealing a significant drop in their ability to recover the shape of the source regions. From the data and figures, our experimental results indicate superior FMT reconstruction outcomes. In the case of multiple light sources, this method can accurately identify the actual positions of multiple sources and exhibits excellent performance in shape recovery, effectively reconstructing the spatial structure of the light sources. Overall, compared to the other three methods, the ROMP-DCP method exhibits the best reconstruction performance in terms of localization accuracy and shape recovery.

3.3.3. *Anti-noise experiment*

To validate the robustness of ROMP-DCP, the following anti-noise experiment was designed. Based on the single-source experiment, where the center coordinate of the light source is (−2, −5, 5) mm, Gaussian noise was successively added at levels of 5 %, 10 %, 15 %, 20 %, and 25 %. Fig. 6 shows the variation of LE and DICE value under different levels of Gaussian noise. Observing the data, we can see that despite the addition of noise, the fluctuations in LE are minimal, stabilizing between 0.3 and 0.4 mm, while the DICE value remains between 0.8 and 0.9. Overall, both the changes in the LE results and the DICE values remain relatively stable. Therefore, the noise resistance experiment results indicate that the ROMP-DCP method exhibits good noise resistance and strong robustness in FMT reconstruction.

3.3.4. *In vivo experiment results*

To further demonstrate the advantages of the ROMP-DCP method, we designed *in vivo* imaging experiments to verify its feasibility in living subjects. The 3D and slice views are shown in Fig. 7. Quantitative analysis of the reconstruction results from the four methods is presented in Table 6. The experimental results indicate that ROMP-DCP achieved the smallest LE at 0.369 mm, while the other three methods showed higher values: IVTCG at 0.544 mm, ROMP at 0.702 mm, and HTPA at 0.962 mm. In terms of shape recovery, the ROMP-DCP algorithm also achieved the highest DICE score, at 0.648, which is approximately 3.57 times greater than that of the HTPA algorithm. This result highlights the effectiveness of ROMP-DCP algorithm in accurately reconstructing source shapes. Compared to other methods, the ROMP-DCP algorithm

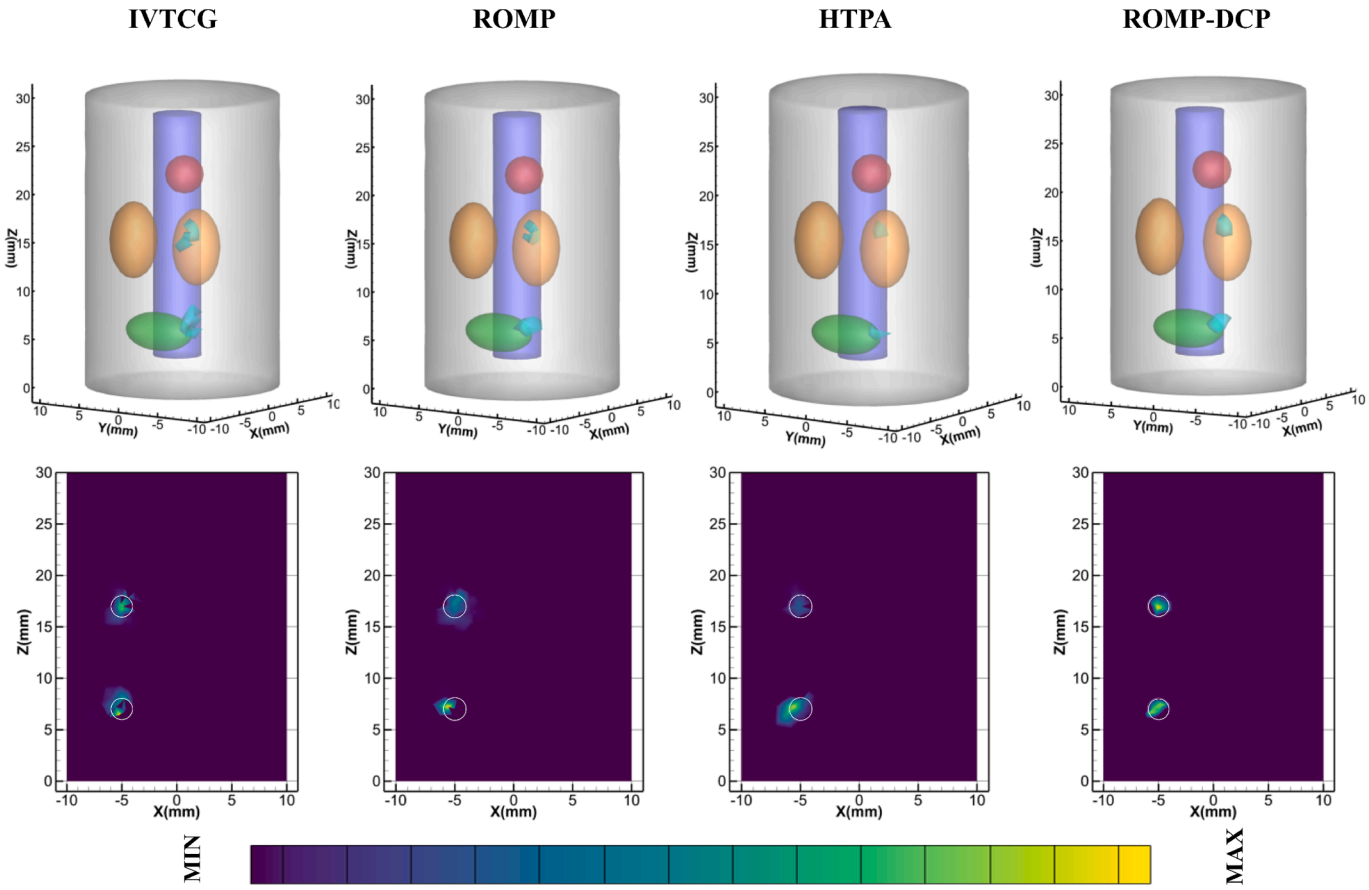

Fig. 5. The reconstruction results of dual-source using four different methods.

Table 5
Quantitative results in dual-source simulation reconstruction experiment.

Method	Actual source center(mm)	Reconstructed source center (mm)	LE (mm)	Total LE (mm)	DICE
IVTCG	(−5, −5, 7) (−5, −5, 17)	(−5.120, −4.856, 7.987) (−4.794, −4.616, 17.226)	1.004 0.491	1.495	0.512 0.449
ROMP	(−5, −5, 7) (−5, −5, 17)	(−5.801, −4.766, 7.108) (−4.712, −4.614, 17.335)	0.842 0.587	1.329	0.480 0.393
HTPA	(−5, −5, 7) (−5, −5, 17)	(−5.943, −4.861, 6.863) (−4.221, −4.154, 17.081)	0.963 1.152	2.115	0.497 0.470
ROMP-DCP	(−5, −5, 7) (−5, −5, 17)	(−5.143, −4.444, 7.105) (−5.042, −4.799, 16.892)	0.583 0.231	0.814	0.600 0.674

demonstrates superior localization accuracy and shape recovery, successfully locating and reconstructing clear shapes of the spatial light sources.

4. Discussion

FMT is a 3D imaging technology that reconstructs molecular distribution images within biological tissues by detecting fluorescently labeled probes. With its high sensitivity and non-invasive property, FMT plays a significant role in tumor research, drug development, and gene expression monitoring. However, due to the severe ill-posedness and instability in the reconstruction process of FMT, the imaging quality is often poor. To address this issue, a sparse reconstruction method for FMT based on the ROMP-DCP approach is proposed in this paper. This method incorporates prior knowledge, such as sparsity priors, to mitigate the ill-posedness of the FMT inverse problem. The ROMP-DCP algorithm integrates the advantages of CS theory and DL techniques, demonstrating exceptional capabilities in sparse representation. It addresses the sparsity of signals and enhances the reconstruction quality by learning the intrinsic structures of data.

The implementation of the ROMP-DCP algorithm is primarily divided into two main phases: a sparse coding phase and a dictionary learning phase. During the sparse coding phase, the ROMP algorithm is utilized, an efficient greedy algorithm employed for selecting atoms most relevant to the fluorescence distribution within an overcomplete dictionary. This method constructs a sparse representation of the fluorescence signals, where each atom corresponds to a significant feature of the distribution. To enhance the accuracy of reconstruction further, regularization constraints are introduced, which control noise and artifacts during the reconstruction process, ensuring the sparsity and robustness of the results. In the dictionary update phase, During the dictionary update phase, DCP and DCA techniques are applied to address the sparse optimization problem of the dictionary. These techniques allow for iterative updates of the dictionary under fixed sparse representation conditions, capturing and learning the intrinsic features of the data more effectively. This process not only optimizes the atoms of the dictionary but also enhances the performance of algorithm by adapting to the specific characteristics of the data. These two phases are iteratively updated alternately to obtain more accurate and sparse reconstruction results of fluorescence distribution.

To verify the effectiveness of the proposed ROMP-DCP method, we designed a series of numerical simulation experiments and *in vivo*

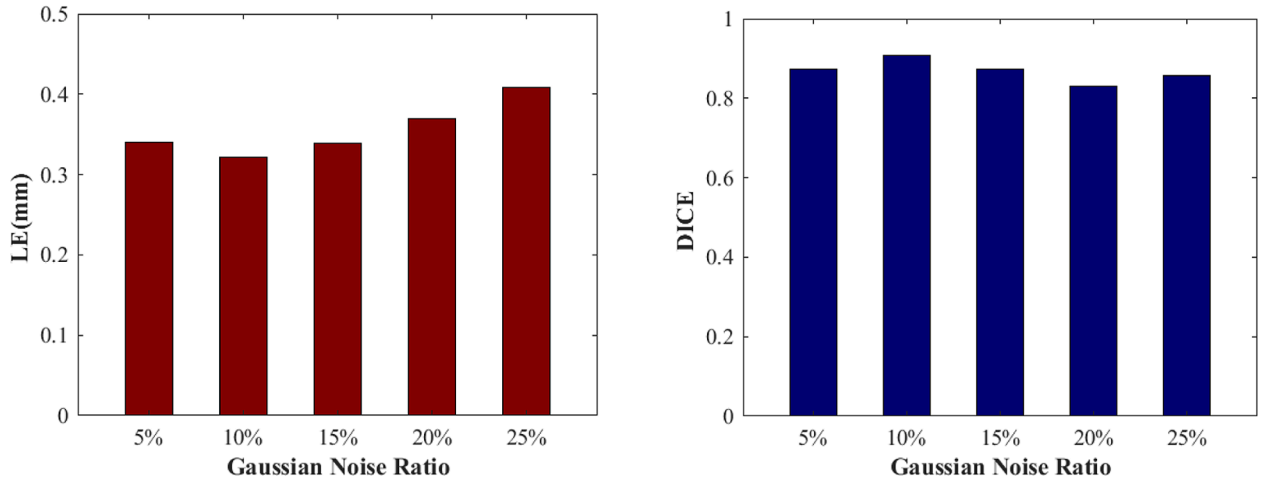

Fig. 6. Results of the anti-noise experiment for FMT single-source reconstruction.

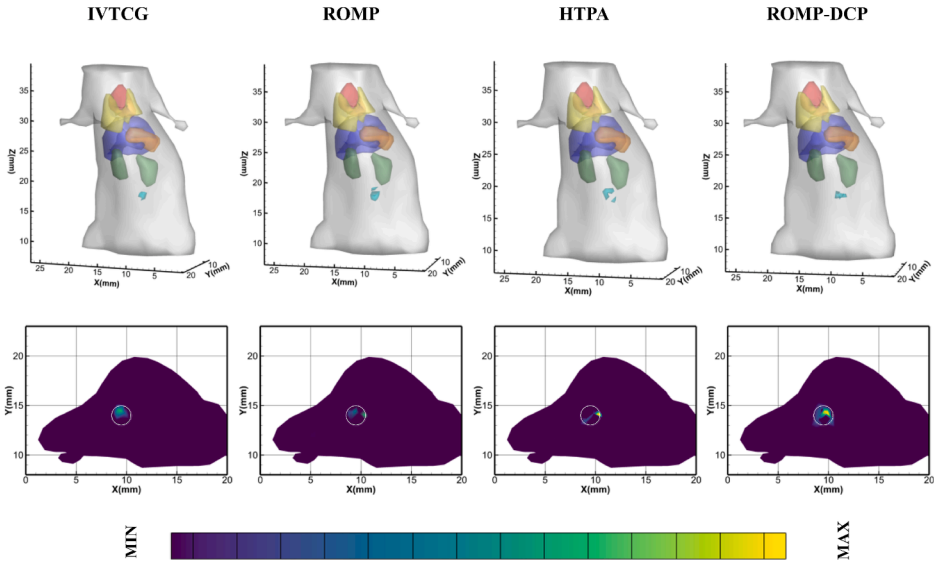

Fig. 7. Reconstruction results of the *in vivo* experiment using four different methods.

Table 6
Quantitative results of the *in vivo* experiment.

Method	Actual source center (mm)	Reconstructed source center (mm)	LE (mm)	DICE
IVTCG	(9.5, 14, 18)	(9.432, 14.508, 17.816)	0.544	0.300
ROMP		(9.981, 14.199, 18.471)	0.702	0.574
HTPA		(10.167, 14.014, 18.693)	0.962	0.182
ROMP-DCP		(9.715, 14.294, 17.939)	0.369	0.648

experiments. We quantitatively compared and analyzed IVTCG, ROMP, HTPA, and ROMP-DCP methods. In the single-source experiment, our proposed ROMP-DCP method achieved the lowest LE of 0.337 mm and the highest DICE value of 0.872. Compared to other methods, ROMP-DCP demonstrated the best reconstruction performance in single-source reconstruction. The dual-source experiment results indicated that ROMP-DCP achieved better reconstruction localization accuracy and shape recovery. In the anti-noise experiments, the results obtained by the ROMP-DCP method showed smaller fluctuations, indicating that this algorithm has strong robustness and stability. To further verify the feasibility and practicality of our proposed ROMP-DCP method, we designed *in vivo* experiments. All experimental results showed that ROMP-DCP has good localization accuracy and shape recovery performance, enabling more accurate reconstruction results.

5. Challenges and future directions

Despite the significant effects achieved by the ROMP-DCP method in FMT, there are still some limitations. Firstly, the sparsity level S determines the number of non-zero elements in the sparse representation, which affects the results of FMT reconstruction. However, the selection of the sparsity level S is currently done manually. While S is a positive integer, simplifying the parameter selection process, we recognize that our method may lack an adaptive mechanism to automatically adjust S based on data. We believe this is an important research direction and plan to explore how to develop such a mechanism in the future to ensure sparse representation while preserving important information. Secondly, based on DCP technique, we developed the DCA. As an iterative algorithm, DCA can result in a long learning process. Therefore, future work will focus on developing more efficient reconstruction algorithms to improve reconstruction speed and computational efficiency, thereby enhancing the feasibility of the algorithm in practical applications.

Furthermore, while the paper primarily focuses on the application of

ROMP-DCP in FMT, we believe that this method has potential applications in other imaging modalities as well. Specifically, FMT shares similarities with X-ray luminescence computed tomography [14], bioluminescence tomography [56], and Cherenkov luminescence tomography [57] in terms of optical properties and sparse representation. The DL strategy in the ROMP-DCP method can effectively capture the sparse features of light sources, which may hold significant value for improving reconstruction algorithms in these other imaging techniques. Therefore, it is necessary to further verify the feasibility and effectiveness of the ROMP-DCP method in other optical tomography imaging techniques. Finally, in this study, we implanted a spherical target in the *in vivo* experiments, because early tumors typically present as spherical. The ROMP-DCP algorithm assumes that tumor is sparse, which theoretically allows for application in early tumor detection. However, we recognize that actual tumor targets may be more complex, including heterogeneous tumors and irregular shapes. Therefore, further research is needed to address these more complex scenarios and improve the proposed method. Future studies will focus on exploring the potential application of this algorithm in preclinical and clinical settings.

6. Conclusion

In conclusion, we proposed a dictionary learning method based on ROMP-DCP to address the FMT inverse problem, achieving significant improvements in FMT reconstruction accuracy. By alternately optimizing the sparse coding and dictionary update stages, the ROMP-DCP method not only ensures sparsity but also demonstrates robustness to noise and optimizes dictionary atoms to obtain stable solutions. We evaluated the performance of our algorithm through a series of numerical simulations and *in vivo* experiments. Compared to IVTCG, ROMP, and HTPA methods, our approach exhibited superior performance in localization accuracy, morphological recovery, and noise robustness. In future work, we aim to refine the ROMP-DCP reconstruction method further by optimizing its computational efficiency and adaptability to more complex tissue structures. Additionally, we will explore its feasibility for clinical applications.

CRediT authorship contribution statement

Linzhi Su: Writing – original draft, Software, Methodology. **Huimin Gao:** Methodology. **Limin Chen:** Resources. **Wenlong Tang:** Validation. **Yi Chen:** Writing – review & editing. **Chengyi Gao:** Conceptualization. **Huangjian Yi:** Validation. **Xin Cao:** Writing – original draft, Supervision.

Declaration of competing interest

The authors declare that they have no known competing financial interests or personal relationships that could have appeared to influence the work reported in this paper.

Acknowledgments

This work was supported in part by the National Major Scientific Research Instrument Development Projects of China (82127805), in part by the Key Research and Development Program of Shaanxi Province (2024SF-YBXM-681), in part by the National Natural Science Foundation of China (61701403, 61806164).

Data availability

Data will be made available on request.

References

[1] R. Weissleder, C.-H. Tung, U. Mahmood, A. Bogdanov, In vivo imaging of tumors with protease-activated near-infrared fluorescent probes, Nat. Biotechnol. 17 (1999) 375–378.
[2] V. Ntziachristos, C. Bremer, R. Weissleder, Fluorescence imaging with near-infrared light: new technological advances that enable in vivo molecular imaging, Eur. Radiol. 13 (2003) 195–208.
[3] C. Chi, Y. Du, J. Ye, D. Kou, J. Qiu, J. Wang, J. Tian, X. Chen, Intraoperative imaging-guided cancer surgery: from current fluorescence molecular imaging methods to future multi-modality imaging technology, Theranostics 4 (2014) 1072.
[4] V. Ntziachristos, Fluorescence molecular imaging, Annu. Rev. Biomed. Eng. 8 (2006) 1–33.
[5] Z. Hu, C. Fang, B. Li, Z. Zhang, C. Cao, M. Cai, S. Su, X. Sun, X. Shi, C. Li, First-in-human liver-tumour surgery guided by multispectral fluorescence imaging in the visible and near-infrared-I/II windows, Nat. Biomed. Eng. 4 (2020) 259–271.
[6] Z. Hu, M. Zhao, Y. Qu, X. Zhang, M. Zhang, M. Liu, H. Guo, Z. Zhang, J. Wang, W. Yang, In vivo 3-dimensional radiopharmaceutical-excited fluorescence tomography, J. Nucl. Med. 58 (2017) 169–174.
[7] Y. An, J. Liu, G. Zhang, J. Ye, Y. Du, Y. Mao, C. Chi, J. Tian, A novel region reconstruction method for fluorescence molecular tomography, IEEE Trans. Biomed. Eng. 62 (2015) 1818–1826.
[8] F. Stuker, J. Ripoll, M. Rudin, Fluorescence molecular tomography: principles and potential for pharmaceutical research, Pharmaceutics 3 (2011) 229–274.
[9] M.A. Whitney, J.L. Crisp, L.T. Nguyen, B. Friedman, L.A. Gross, P. Steinbach, R. Y. Tsien, Q.T. Nguyen, Fluorescent peptides highlight peripheral nerves during surgery in mice, Nat. Biotechnol. 29 (2011) 352–356.
[10] X. Shi, Z. Zhang, Z. Zhang, C. Cao, Z. Cheng, Z. Hu, J. Tian, N. Ji, Near-infrared window II fluorescence image-guided surgery of high-grade gliomas prolongs the progression-free survival of patients, IEEE Trans. Biomed. Eng. 69 (2021) 1889–1900.
[11] E. Fang, J. Wang, D. Hu, J. Zhang, W. Zou, Y. Zhou, Adaptive monotone fast iterative shrinkage thresholding algorithm for fluorescence molecular tomography, IET Sci. Meas. Technol. 9 (2015) 587–595.
[12] F. Liu, X. Liu, B. Zhang, J. Bai, Extraction of target fluorescence signal from in vivo background signal using image subtraction algorithm, Int. J. Autom. Comput. 9 (2012) 232–236.
[13] C. Darne, Y. Lu, E.M. Sevick-Muraca, Small animal fluorescence and bioluminescence tomography: a review of approaches, algorithms and technology update, Phys. Med. Biol. 59 (2013) R1.
[14] Y. Chen, M. Du, G. Zhang, J. Zhang, K. Li, L. Su, F. Zhao, H. Yi, X. Cao, Sparse reconstruction based on dictionary learning and group structure strategy for cone-beam X-ray luminescence computed tomography, Opt Express 31 (2023) 24845–24861.
[15] P. Zhang, C. Ma, F. Song, G. Fan, Y. Sun, Y. Feng, X. Ma, F. Liu, G. Zhang, A review of advances in imaging methodology in fluorescence molecular tomography, Phys Med Biol 67 (2022).
[16] M.F. Kircher, A. De La Zerda, J.V. Jokerst, C.L. Zavaleta, P.J. Kempen, E. Mittra, K. Pitter, R. Huang, C. Campos, F. Habte, A brain tumor molecular imaging strategy using a new triple-modality MRI-photoacoustic-Raman nanoparticle, Nat. Med. 18 (2012) 829–834.
[17] Y. Zhou, M. Chen, H. Su, J. Luo, Self-prior strategy for organ reconstruction in fluorescence molecular tomography, Biomed. Opt. Express 8 (2017) 4671–4686.
[18] H. Meng, K. Wang, Y. Gao, Y. Jin, X. Ma, J. Tian, Adaptive Gaussian Weighted Laplace Prior Regularization Enables Accurate Morphological Reconstruction in Fluorescence Molecular Tomography, IEEE Trans. Med. Imaging 38 (2019) 2726–2734.
[19] D. Han, X. Yang, K. Liu, C. Qin, B. Zhang, X. Ma, J. Tian, Efficient reconstruction method for L1 regularization in fluorescence molecular tomography, Appl. Opt. 49 (2010) 6930–6937.
[20] H. Zhang, X. He, J. Yu, X. He, H. Guo, Y. Hou, L1-L2 norm regularization via forward-backward splitting for fluorescence molecular tomography, Biomed. Opt. Express 12 (2021) 7807–7825.
[21] D. Han, J. Tian, S. Zhu, J. Feng, C. Qin, B. Zhang, X. Yang, A fast reconstruction algorithm for fluorescence molecular tomography with sparsity regularization, Opt. Express 18 (2010) 8630–8646.
[22] X. Chen, D. Yang, Q. Zhang, J. Liang, L1/2 regularization based numerical method for effective reconstruction of bioluminescence tomography, J. Appl. Phys. 115 (2014).
[23] X. He, H. Meng, X. He, K. Wang, X. Song, J. Tian, Nonconvex laplacian manifold joint method for morphological reconstruction of fluorescence molecular tomography, Mol. Imag. Biol. 23 (2021) 394–406.
[24] F. Long, Deep learning-based mesoscopic fluorescence molecular tomography: an in silico study, J. Med. Imaging 5 (2018) 036001.
[25] L. Guo, F. Liu, C. Cai, J. Liu, G. Zhang, 3D deep encoder-decoder network for fluorescence molecular tomography, Opt. Lett. 44 (2019) 1892–1895.
[26] C. Huang, H. Meng, Y. Gao, S. Jiang, K. Wang, J. Tian, Fast and robust reconstruction method for fluorescence molecular tomography based on deep neural network, in *Imaging, Manipulation, and Analysis of Biomolecules, Cells, and Tissues XVII*(SPIE2019), pp. 257–262.
[27] P. Zhang, G. Fan, T. Xing, F. Song, G. Zhang, UHR-DeepFMT: ultra-high spatial resolution reconstruction of fluorescence molecular tomography based on 3-D fusion dual-sampling deep neural network, IEEE Trans Med Imaging 40 (2021) 3217–3228.
[28] V. Michel, R. Telschow, The regularized orthogonal functional matching pursuit for ill-posed inverse problems, Siam J Numer Anal 54 (2016) 262–287.

[29] L. Kong, Y. An, Q. Liang, L. Yin, Y. Du, J. Tian, Reconstruction for fluorescence molecular tomography via adaptive group orthogonal matching pursuit, IEEE Trans. Biomed. Eng. 67 (2020) 2518–2529.
[30] Y. Rong, S. Xiong, Y. Gao, Double graph regularized double dictionary learning for image classification, IEEE Trans. Image Process. 29 (2020) 7707–7721.
[31] P. Song, L. Weizman, J.F. Mota, Y.C. Eldar, M.R. Rodrigues, Coupled dictionary learning for multi-contrast MRI reconstruction, IEEE Trans. Med. Imaging 39 (2019) 621–633.
[32] Z. Li, C. Wan, B. Tan, Z. Yang, S. Xie, A fast DC-based dictionary learning algorithm with the SCAD penalty, Neurocomputing 429 (2021) 89–100.
[33] X. Li, S. Ding, Z. Li, B. Tan, Device-free localization via dictionary learning with difference of convex programming, IEEE Sens. J. 1–1 (2017).
[34] X. T. Vo, H. An Le Thi, T. P. Dinh, T. B. T. Nguyen, DC programming and DCA for dictionary learning, in *Computational Collective Intelligence: 7th International Conference, ICCCI 2015, Madrid, Spain, September 21-23, 2015, Proceedings, Part I* (Springer2015), pp. 295–304.
[35] A.D. Klose, V. Ntziachristos, A.H. Hielscher, The inverse source problem based on the radiative transfer equation in optical molecular imaging, J. Comput. Phys. 202 (2005) 323–345.
[36] G. Zhang, H. Pu, W. He, F. Liu, J. Luo, J. Bai, Full-direct method for imaging pharmacokinetic parameters in dynamic fluorescence molecular tomography, Appl. Phys. Lett. 106 (2015).
[37] S. Jiang, J. Liu, G. Zhang, Y. An, H. Meng, Y. Gao, K. Wang, J. Tian, Reconstruction of fluorescence molecular tomography via a fused LASSO method based on group sparsity prior, IEEE Trans Biomed Eng 66 (2019) 1361–1371.
[38] A.D. Klose, E.W. Larsen, Light transport in biological tissue based on the simplified spherical harmonics equations, J. Comput. Phys. 220 (2006) 441–470.
[39] S.L. Jacques, Optical properties of biological tissues: a review, Phys. Med. Biol. 58 (2013) R37.
[40] G. Gasso, A. Rakotomamonjy, S. Canu, Recovering sparse signals with a certain family of nonconvex penalties and DC programming, IEEE Trans. Signal Process. 57 (2009) 4686–4698.
[41] K. Tono, A. Takeda, J.-y. Gotoh, Efficient DC algorithm for constrained sparse optimization, arXiv preprint arXiv:1701.08498 (2017).
[42] Z. Li, Z. Yang, H. Zhao, S. Xie, Direct-optimization-based DC dictionary learning with the MCP regularizer, IEEE Trans. Neural Networks Learn. Syst. 34 (2023) 3568–3579.
[43] Y. Yuan, H. Yi, D. Kang, J. Yu, H. Guo, X. He, X. He, Robust transformed l(1) metric for fluorescence molecular tomography, Comput. Methods Programs. Biomed. 234 (2023) 107503.
[44] H.A. Le Thi, T.P. Dinh, H.M. Le, X.T. Vo, DC approximation approaches for sparse optimization, Eur. J. Oper. Res. 244 (2015) 26–46.
[45] H.A. Le Thi, T. Pham Dinh, Open issues and recent advances in DC programming and DCA, J. Glob. Optim. 88 (2024) 533–590.
[46] T. Pham Dinh, H.A. Le Thi, Recent advances in DC programming and DCA, in: Transactions on Computational Intelligence XIII, 2014, pp. 1–37.
[47] L.T.H. An, P.D. Tao, The DC (difference of convex functions) programming and DCA revisited with DC models of real world nonconvex optimization problems, Ann. Oper. Res. 133 (2005) 23–46.
[48] P.D. Tao, L.H. An, Convex analysis approach to DC programming: theory, algorithms and applications, Acta Math. Vietnam. 22 (1997) 289–355.
[49] S. Jiang, J. Liu, Y. An, Y. Gao, H. Meng, K. Wang, J. Tian, Fluorescence molecular tomography based on group sparsity priori for morphological reconstruction of glioma, IEEE Trans. Biomed. Eng. 67 (2020) 1429–1437.
[50] D. Needell, R. Vershynin, Signal recovery from incomplete and inaccurate measurements via ROMP, (Citeseer, 2013).
[51] X. He, J. Liang, X. Wang, J. Yu, X. Qu, X. Wang, Y. Hou, D. Chen, F. Liu, J. Tian, Sparse reconstruction for quantitative bioluminescence tomography based on the incomplete variables truncated conjugate gradient method, Opt. Express 18 (2010) 24825–24841.
[52] X. He, J. Yu, X. Wang, H. Yi, Y. Chen, X. Song, X. He, Half thresholding pursuit algorithm for fluorescence molecular tomography, IEEE Trans. Biomed. Eng. 66 (2019) 1468–1476.
[53] Y. Hou, X. Hua, C. Xin, H. Zhang, Q. Xuan, X. He, Single-view enhanced cerenkov luminescence tomography based on sparse bayesian learning, Acta Opt. Sin. 37 (2017) 298–308.
[54] E.J. Dickinson, H. Ekström, E. Fontes, COMSOL Multiphysics®: Finite element software for electrochemical analysis. A mini-review, Electrochem. Commun. 40 (2014) 71–74.
[55] H. Li, J. Tian, F. Zhu, W. Cong, L.V. Wang, E.A. Hoffman, G. Wang, A mouse optical simulation environment (MOSE) to investigate bioluminescent phenomena in the living mouse with the monte carlo method1, Acad. Radiol. 11 (2004) 1029–1038.
[56] Y. Wang, H. Zhang, H. Guo, B. Wang, Y. Liu, X. He, J. Yu, H. Yi, X. He, Accurate and fast reconstruction for bioluminescence tomography based on adaptive Newton hard thresholding pursuit algorithm, JOSA A 39 (2022) 829–840.
[57] Y. Chen, W. Li, M. Du, L. Su, H. Yi, F. Zhao, K. Li, L. Wang, X. Cao, Elastic net-based non-negative iterative three-operator splitting strategy for Cerenkov luminescence tomography, Opt. Express 30 (2022).